

Article

# Enhanced Efficiency on ANPC-DAB through Adaptive Model Predictive Control

Adriano Nardoto <sup>1</sup>, Lucas Encarnação <sup>2,\*</sup>, Walbermark Santos <sup>2</sup>, Arthur Amorim <sup>1</sup>, Rodrigo Fiorotti <sup>1</sup>, David Molinero <sup>3</sup> and Emilio Bueno <sup>3</sup>

<sup>1</sup> Department of Electrical Engineering, Federal Institute of Espírito Santo (IFES), BR101 Km 58, São Mateus 29932-540, Brazil; adriano.nardoto@ifes.edu.br (A.N.); arthur.amorim@ifes.edu.br (A.A.); rodrigo.fiorotti@ifes.edu.br (R.F.)

<sup>2</sup> Department of Electrical Engineering, Federal University of Espírito Santo (UFES), Av. Fernando Ferrari, 514, Vitória 29075-910, Brazil; walbermark.santos@ufes.br

<sup>3</sup> Department of Electronics, Alcalá University (UAH), Plaza San Diego S/N, 28801 Madrid, Spain; david.molinero@uah.es (D.M.); emilio.bueno@uah.es (E.B.)

\* Correspondence: lucas.encarnacao@ufes.br

**Abstract:** This work studies the DC-DC conversion stage in solid-state transformers (SST). The traditional two- or three-level dual active bridge (DAB) topology faces limitations in microgrid interconnection due to power and voltage limitations. For this reason, the use of multilevel topologies such as active neutral point clamped (ANPC) is a promising alternative. Additionally, the efficiency of the SSTs is a recurring concern, and reducing losses in the DC-DC stage is a subject to be studied. In this context, this work presents a new control technique based on an adaptive model-based predictive control (AMPC) to select the modulation technique of an ANPC-DAB DC-DC converter aimed at reducing losses and increasing efficiency. The single-phase shift (SPS), triangular, and trapezoidal modulation techniques are used according to the converter output power with the aim of maximizing the number of soft-switching points per cycle. The performance of the proposed control technique is demonstrated through real-time simulation and a reduced-scale experimental setup. The findings indicate the effectiveness of the AMPC control technique in mitigating voltage source perturbations. This technique has low output impedance and is robust to converter parameter variations. Prototyping tests revealed that, in steady-state, the AMPC significantly improves converter efficiency without compromising dynamic performance. Despite its advantages, the computational cost of AMPC is not significantly higher than that of traditional model predictive control (MPC), allowing for the allocation of time to other applications.

**Keywords:** Dual Active Bridge (DAB) converter; active neutral point clamped (ANPC); model predictive control (MPC); power electronics; switching losses; adaptive control



**Citation:** Nardoto, A.; Encarnação, L.; Santos, W.; Amorim, A.; Fiorotti, R.; Molinero, D.; Bueno, E. Enhanced Efficiency on ANPC-DAB through Adaptive Model Predictive Control. *Energies* **2024**, *17*, 12. <https://doi.org/10.3390/en17010012>

Academic Editor: Ahmed Abu-Siada

Received: 14 November 2023

Revised: 4 December 2023

Accepted: 8 December 2023

Published: 19 December 2023



**Copyright:** © 2023 by the authors. Licensee MDPI, Basel, Switzerland. This article is an open access article distributed under the terms and conditions of the Creative Commons Attribution (CC BY) license (<https://creativecommons.org/licenses/by/4.0/>).

## 1. Introduction

The solid-state transformer (SST) is becoming an important technology and is foundational to applications that include traction systems, offshore energy generation, DC grids and especially microgrids. Its advantages, such as accurate output-voltage regulation, short-circuit current limitation, power factor compensation, reduced weight and volume in comparison with traditional transformers, and voltage-dip immunity under certain limitations, enable the construction of a new paradigm in electric power systems [1].

The future of the electric power system seems to be a smart grid with power-flow management, incorporated energy storage systems, quick transient response and high integration of renewable energy [2]. All of these features can be incorporated through the utilization of SST. However, this device still has opportunities for improvement, mainly related to cost reduction, reliability, and efficiency [3].

The usual topology of the SST is presented in Figure 1. It shows the AC-DC conversion (Stage 1), DC-DC conversion (Stage 2), and DC-AC conversion (Stage 3), with the high-voltage utility grid on the left and the low-voltage microgrid on the right and all stages allowing bidirectional power flow. Stage 2 traditionally employs a DC-DC converter through a resonant magnetic link to connect high-voltage DC to low-voltage DC, and the efficiency of SST is closely related to losses in this stage.

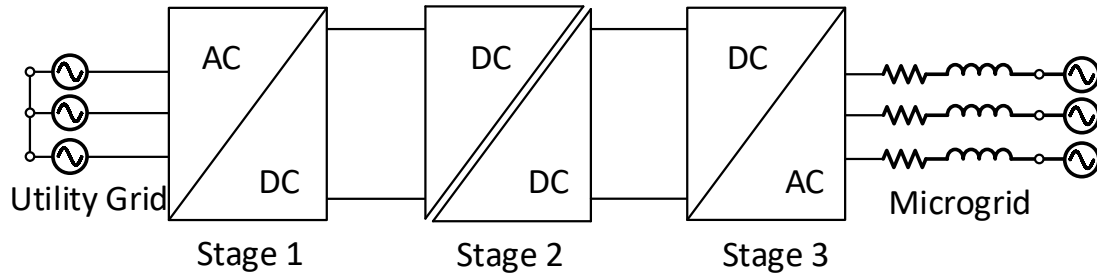


Figure 1. SST Topology.

The dual active bridge (DAB) is the general term for the isolated converter formed by the union of two active bridges through an inductor and a high-frequency transformer.

The requirements for building a DAB controller are a fast transient response, minimum steady-state error and reduced losses on the power converter. Hence, an adaptive model predictive control (AMPC) is proposed for a DAB converter in this work. The topology adopted in this work is shown in Figure 2 and operates with an active neutral point clamped (ANPC) converter on the high-voltage side and a H-bridge on the low-voltage side. In this work, it is referred to as ANPC-DAB. Its performance is evaluated through a 8 kW prototype.

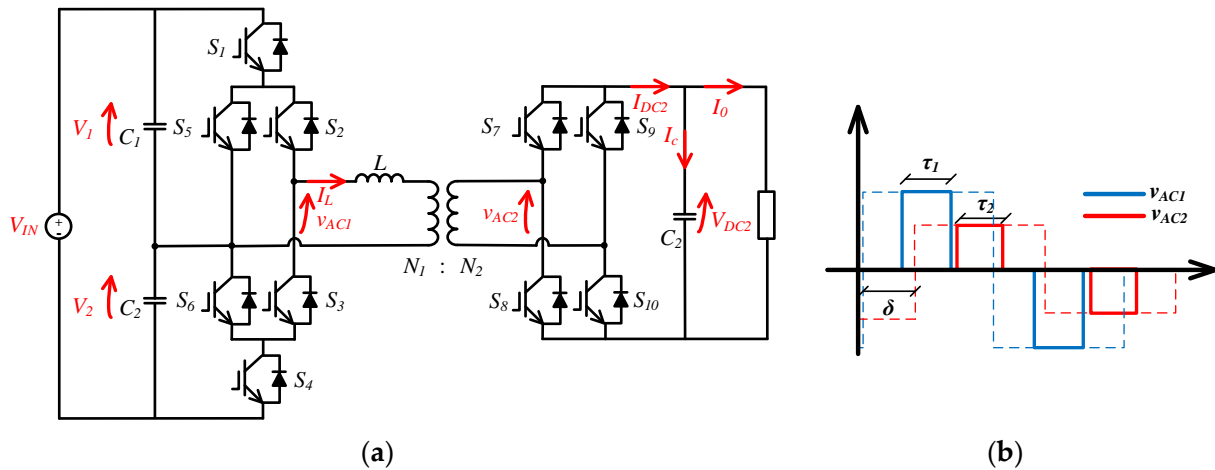


Figure 2. DAB Converter (a) ANPC-DAB topology (b) Three-level voltages,  $v_{AC1}$  and  $v_{AC2}$ .

1.1. Literature Review

1.1.1. DAB Converter Topology

The H-bridge two-level DAB is the most commonly used topology for Stage 2 of an SST. Despite the many advantages of this structure, it is unable to deal with high power and high voltage, being limited by semiconductor technology.

The main solution to this difficulty is the series and parallel connection of the converters; however, additional challenges arise in equalizing voltages and sharing currents. Another alternative is the cascade connection of multiple DAB converters, which increases the number of power switches and the complexity of the control scheme. Hence, the utilization of multilevel structures seems to be the best solution. Many multilevel structures

have been widely used with success. Various three-level (3L) topologies have been applied to the DAB converter: flying capacitor, neutral point clamped (NPC), and ANPC [4].

The NPC topology is still widely employed in the industrial sector, notably for operating medium-voltage electric motors [5]. However, the 3L-NPC has some limitations that affect its performance. Some of the switches must withstand higher voltages than others [6], and the power loss in each semiconductor is highly unbalanced [6].

The ANPC converter was proposed to overcome these problems by replacing the clamping diodes with active switches generating redundant switching stages [7]. These redundant stages are used to equalize the voltage and reduce unbalanced losses in each switch, increasing the power-processing capacity of the converter.

### 1.1.2. Modulation Techniques for Loss Reduction

Traditionally, the single-phase shift (SPS) modulation is used in DAB converters. The main advantage of this strategy is that it allows for zero voltage switching (ZVS) over a wide operating range [8]. However, when the relationship between the input and output voltage is far from unity, especially under small loads, these soft-switching techniques are not possible. Additionally, the converter experiences significant backflow-power in this scenario, leading to high circulating currents and increased stress on the switches and conduction losses. In conclusion, the SPS modulation may not ensure high efficiency of the DAB converter over its entire operating range.

A previous work has shown the improvements obtained through the utilization of trapezoidal and triangular modulation techniques [9,10]. These techniques can naturally extend the DAB's soft-switching operation and consist of the utilization of pulse widths different from 50% [11]. Their proper application can increase the number of soft commutations to four (for trapezoidal modulation) or six (for triangular modulation) out of a total of eight in a cycle, even during operation with reduced loads.

In the AC-DC conversion literature, various balancing control strategies have been proposed to optimize the loss distribution of the ANPC circuit [7,12,13]. The voltage synthesized by the rectifier takes on  $V_{DC}$  ( $P$ ) or zero ( $Z$ ) during the positive cycle of the electrical grid, resulting in  $P \leftrightarrow Z$  type commutations for half of the grid period. During the negative cycle of the electrical grid, the voltage synthesized by the rectifier takes on  $-V_{DC}$  ( $N$ ) or zero ( $Z$ ), resulting in  $N \leftrightarrow Z$  type commutations for the other half of the grid period. However, in the case of the DAB converter, the ANPC bridge losses distribution is carried out at each sampling time, with  $P \leftrightarrow Z \leftrightarrow N$  switches occurring within each sampling period. As a result, all six switches are used within each switching period of the DAB converter.

The literature includes studies on ANPC-DAB switching for loss distribution among the converter switches. Some states involving the transition between the current path through the clamping diode and through the active switch of the converter are presented in [4]. In [14], a modulation is proposed to minimize the number of switching actions, realizing the ZVS turn-ON for all switches and avoiding hard switching turn-OFF in specific switches. In [15], the electromagnetic interference (EMI) caused by zero voltage switching in the ANPC-DAB converter was evaluated.

### 1.2. Contributions

The literature review revealed that work on DAB converters can be divided into two groups. The first group involves the development of modulation strategies to enhance the efficiency of the power converter, while the second group deals with novel control techniques to improve the transient and steady-state response. In this paper, both goals are pursued simultaneously through a novel scheme pf control and modulation.

The control proposal was developed to manage the DAB converter and is based on model predictive control (MPC), which incorporates a variable phase-shift adjustment depending on the error between the desired value and the measured variable. However, it has been enhanced for AMPC control. In this new configuration, the control is capable

of selecting operation modes (trapezoidal and triangular) in order to minimize losses and thus enhance converter efficiency. The proposed AMPC is applied to an ANPC-DAB, and the results are validated through an experimental setup.

Going beyond previously published work found in the literature, this analysis includes the following: the utilization of a realistic switching frequency (20 kHz); a compensation scheme for the AMPC delay; tests with load disturbance rejection; an improved cost function that considers capacitor discharge; and a quantitative study of the influence of parameter variation.

### 1.3. Paper Organization

The paper is organized as follows: Section 2 presents the mathematical modeling of the SPS and the triangular and trapezoidal modulations. The proposed control scheme is detailed in Section 3. Section 4 shows the results of the computational simulation. The experimental results are shown and discussed in Section 5. Finally, Section 6 shows the conclusions of this work.

## 2. ANPC-DAB Topology and Modulations

The DAB converter is formed by two active bridges connected through a high-frequency transformer. In this study, an ANPC converter is used on the high-voltage side, operating as an inverter. There is an H-bridge on the low-voltage side, operating as a rectifier. Together, they form the ANPC-DAB topology, as shown in Figure 2a.

Figure 2b shows a generic representation of the three-level voltages  $v_{AC1}$  and  $v_{AC2}$  synthesized by the active bridges using a centralized PWM. The dashed line represents the voltage generated by SPS modulation. The phase shift  $\delta$  and inner phase shift  $\tau_1$  and  $\tau_2$  are defined in Equation (1):

$$\begin{cases} -90^\circ < \delta < 90^\circ \\ 0 < \tau_1 < 180^\circ \\ 0 < \tau_2 < 180^\circ \end{cases} \quad (1)$$

One of the fundamental characteristics of the DAB converter is its ability to operate with ZVS in a large part of its operating range when operating in SPS modulation [8,16], and this ability can be extended to the entire operating range when using modulations with greater degrees of freedom [17,18].

The ZVS conditions of the ANPC-DAB are consistent with the ZVS conditions of a dual H-bridge DAB [4,14]. Thus, when they use the same phase-angle shift modulation method, the ANPC-DAB, DNPC-DAB, and H-bridge DAB circuits have the same phase-shift ranges for the ZVS of all switches [19].

The next section analyzes the switching used in the ANPC-DAB converter. Section 2.2 contains an analysis of the operating points at which the ZVS occurs in the SPS modulation. Section 2.3 contains an analysis of the ZVS involving triangular and trapezoidal modulations, the basis of AMPC.

### 2.1. ANPC-DAB State Switching

The 3L-ANPC topology has one active switch connected in parallel with each clamp diode. These two switches allow the AC terminal to be connected to the midpoint DC link (neutral point) in more than one switching state. The four resultant zero states are presented in Table 1 and described as  $Z_{OH1}$ ,  $Z_{OH2}$ ,  $Z_{OL1}$ , and  $Z_{OL2}$ . This configuration allows for a more even distribution of switch losses in the converter, increasing its energy-processing capacity.

**Table 1.** Switching sequences of the 3L-ANPC converter.

AC Side	Switching State	Switch Sequence					
		$S_1$	$S_2$	$S_3$	$S_4$	$S_5$	$S_6$
$V_{DC1}$	$P$	1	1	0	0	0	1
0	$Z_{OH1}$	0	1	0	1	1	0
0	$Z_{OH2}$	0	1	0	0	1	0
0	$Z_{OL1}$	1	0	1	0	0	1
0	$Z_{OL2}$	0	0	1	0	0	1
$-V_{DC2}$	$N$	0	0	1	1	1	0

The switching scheme used in this work is shown in Figure 3. The  $v_{AC1}$  and  $v_{AC2}$  voltage synthesized and the trigger pulses on the switches for both sides of converter are own, highlighting the positive cycle in red and the negative cycle in blue.

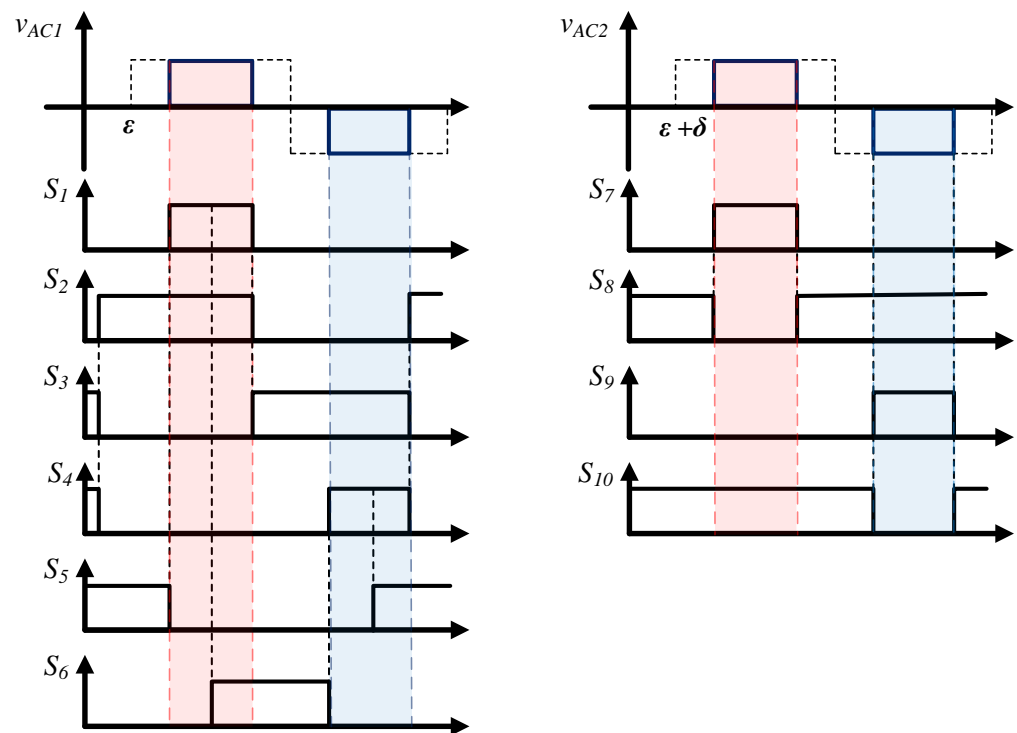


**Figure 3.** Voltage and the trigger pulses on the switches for both sides of the converter. The red color indicates the moments in time when  $v_{AC1}$  and  $v_{AC2}$  are positive, while the blue color indicates the moments when  $v_{AC1}$  and  $v_{AC2}$  are negative.

## 2.2. SPS Modulation

SPS modulation is the main modulation used by the ANPC-DAB converter. The only control variable is the phase shift, that is,  $\tau_1 = \tau_2 = 180^\circ$ . In this work, the voltages on the ANPC-DAB input capacitors will be the same, that is,  $V_1 = V_2 = V_{DC1}$ . The power transferred using SPS modulation, for a given operating point, is shown in (2).

$$P_{SPS} = \frac{4 \cdot n \cdot V_{DC1} \cdot V_{DC2} \cdot \sin \delta}{\pi^3 \cdot f_{sw} \cdot L} \quad (2)$$

where  $L$  is power transfer inductance;  $n$  is the transformer ratio ( $n = N_1/N_2$ );  $f_{sw}$  is the switching frequency of the converter; and  $V_{DC1}$  and  $V_{DC2}$  are the input and output voltage on capacitors, respectively.

The power boundaries for the ZVS actuation of the primary and secondary active bridges are presented in (3). If the DAB’s power is above  $P_{ZVS2}$  or below  $P_{ZVS1}$ , the DAB converter cannot operate with ZVS [20].

$$\begin{cases} P_{ZVS1} = \left( \frac{V_{DC1}^2 \cdot \delta}{2 \cdot \pi \cdot f_{sw} \cdot L \cdot \Phi} \right) \cdot \left( \frac{\pi - |\delta|}{\pi - 2 \cdot |\delta|} \right) \\ P_{ZVS2} = \left( \frac{V_{DC1}^2 \cdot \delta}{2 \cdot \pi \cdot f_{sw} \cdot L \cdot \Phi} \right) \cdot \left( \frac{\pi - |\delta|}{\pi} \right) \cdot \left( \frac{\pi - 2 \cdot |\delta|}{\pi} \right) \end{cases} \quad (3)$$

where  $\Phi$  is the rated phase shift.

The DAB transformation ratio  $d$  is defined in (4). When  $d = 1$ , the DAB operates in ZVS over the whole power range. When  $d > 1$ , the primary bridge operates with hard switching. When  $d < 1$ , the secondary bridge operates with hard switching.

$$d = \frac{N_1 \cdot V_{DC2}}{N_2 \cdot V_{DC1}} \quad (4)$$

Figure 4 shows the DAB power curve as a function of various values of  $d$  to highlight the ZVS region. The solid blue and red lines indicate the power limits within which the primary and secondary bridges, respectively, can operate in soft switching. The solid black line represents  $d = 1$ , where the converter operates in soft switching. The dashed lines show the operating points for  $d \neq 1$ . For this analysis, we assumed that  $\Phi = 45^\circ$ .

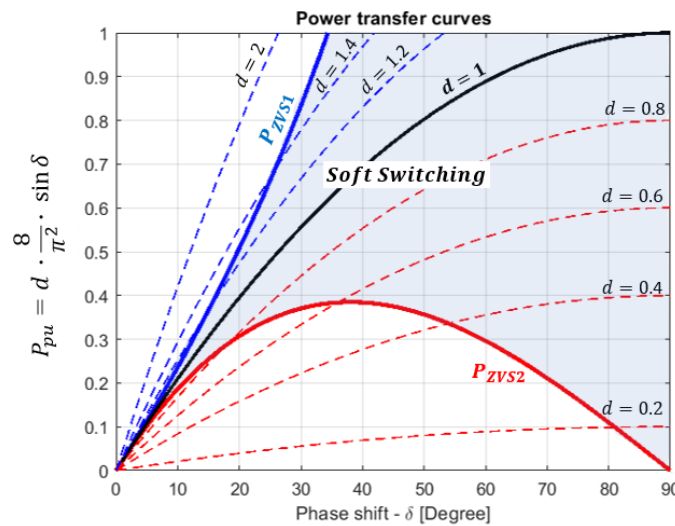


Figure 4. Power transfer curves and limit powers for ZVS operation.

These curves show that small phase shifts and significant deviations from unity in the DAB transformation ratio make it difficult to operate the converter in ZVS and decrease its efficiency at those points. Thus, SPS modulation is insufficient to ensure high-efficiency operation of the DAB converter over its entire operational range.

### 2.3. Triangular and Trapezoidal Modulation

An alternative method by which to extend soft switching to regions where SPS modulation does not allow ZVS operation is to apply triangular and trapezoidal modulation.

Triangular modulation has the advantage of allowing soft switching on six transitions, for a total of eight switchings. However, it cannot be used over the entire operating range of the converter because its power transmission capacity is limited, and it is possible to transfer power only when  $d \neq 1$ .

When  $d < 1$ , the phase shift  $\delta$  and inner phase shift  $\tau_1$  and  $\tau_2$  are calculated so that the current in the inductor  $I_L$  is zero when there are simultaneous changes of state:  $Z \rightarrow P$  in the primary and secondary bridge and  $P \rightarrow Z$  in the secondary bridge. When  $d > 1$ , the phase shift  $\delta$  and inner phase shift  $\tau_1$  and  $\tau_2$  are calculated so that the current in the

inductor  $I_L$  is zero when there are simultaneous changes of state:  $Z \rightarrow P$  in the primary bridge and  $P \rightarrow Z$  in the primary and secondary bridges. In the negative half-cycle, the procedure is repeated, replacing  $P$  with  $N$ . Figure 5 shows the waveforms of the voltages  $v_{AC1}$  and  $n \cdot v_{AC2}$  on the active bridges and the inductor current  $I_L$ .

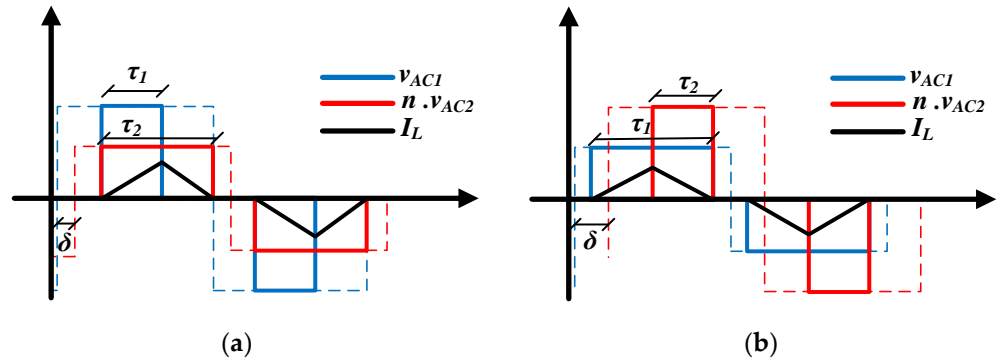


Figure 5. Voltage and current waveforms for triangular modulation (a)  $d < 1$  (b)  $d > 1$ .

The values of the inner phase shift  $\tau_1$  and  $\tau_2$  for the triangular modulation are calculated from the voltages and phase shift. When  $d < 1$ , the calculation is done as shown in (5). When  $d > 1$ , the calculation is done as shown in (6).

$$\begin{cases} \tau_1 = 2 \cdot \delta \cdot \left( \frac{n \cdot V_{DC2}}{V_{DC1} - n \cdot V_{DC2}} \right) \\ \tau_2 = 2 \cdot \delta \cdot \left( \frac{V_{DC1}}{V_{DC1} - n \cdot V_{DC2}} \right) \end{cases} \quad (5)$$

$$\begin{cases} \tau_1 = 2 \cdot \delta \cdot \left( \frac{n \cdot V_{DC2}}{n \cdot V_{DC2} - V_{DC1}} \right) \\ \tau_2 = 2 \cdot \delta \cdot \left( \frac{V_{DC1}}{n \cdot V_{DC2} - V_{DC1}} \right) \end{cases} \quad (6)$$

When triangular modulation cannot supply the necessary power for a given operating point, trapezoidal modulation is used. Trapezoidal modulation is an extension of triangle modulation, which ensures smooth transition between modulations [11]. In addition, soft switching occurs in four out of the eight switchings per cycle. Moreover, this modulation is possible for any value of  $d$ . Figure 6 shows the waveforms of the voltages  $v_{AC1}$  and  $n \cdot v_{AC2}$  on the active bridges and the inductor current  $I_L$  for the trapezoidal modulation.

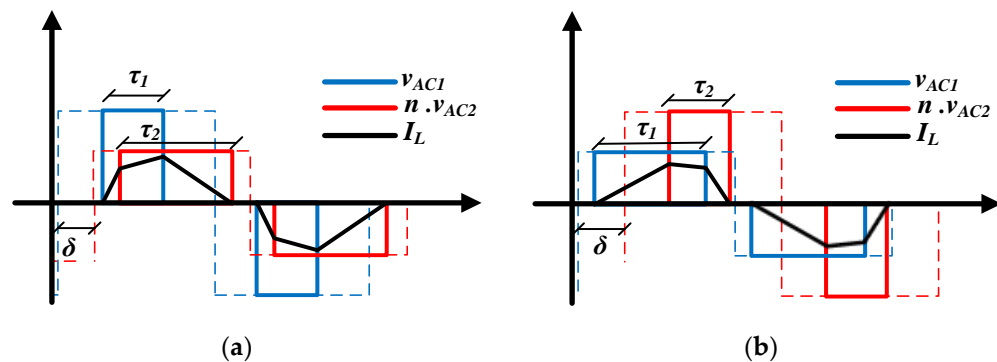
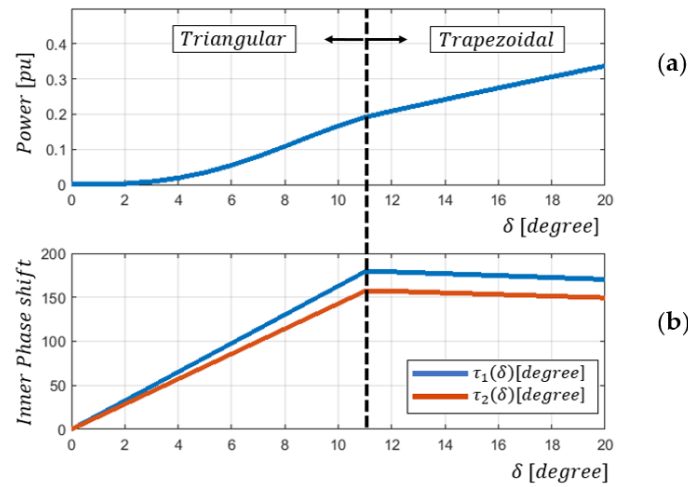


Figure 6. Voltage and current waveforms for trapezoidal modulation (a)  $d < 1$  (b)  $d > 1$ .

The values of the inner phase shift  $\tau_1$  and  $\tau_2$  for the trapezoidal modulation are calculated from the voltages and phase shift, as shown in (7).

$$\begin{cases} \tau_1 = 2 \cdot (\pi - \delta) \cdot \left( \frac{n \cdot V_{DC2}}{n \cdot V_{DC2} + V_{DC1}} \right) \\ \tau_2 = 2 \cdot (\pi - \delta) \cdot \left( \frac{V_{DC1}}{n \cdot V_{DC2} + V_{DC1}} \right) \end{cases} \quad (7)$$

The natural transition between triangular and trapezoidal modulations is shown in Figure 7a, where the power transferred by the converter is plotted as a function of the phase shift,  $\tau_1$  and  $\tau_2$ . Figure 7b shows the values of  $\tau_1$  and  $\tau_2$  as a function of  $\delta$ .



**Figure 7.** Natural transition between triangular and trapezoidal modulations (a) Power transferred by the converter as a function of the phase shift  $\delta$  (b) Values of  $\tau_1$  and  $\tau_2$  as a function of delta  $\delta$ .

### 3. Proposed Adaptive Model Predictive Control (AMPC)

In power electronics, contemporary control methods are frequently employed. MPC is one notable example.

Control methodologies that aim to reduce switching losses in the converter usually require complex algorithms to define the three control variables ( $\delta$ ,  $\tau_1$  and  $\tau_2$ ) to achieve the desired output voltage. In a deviation from these methods, the AMPC control uses triangular and trapezoidal modulations to reduce switching losses in the converter. The control defines the modulation to be used according to the converter operating point. The great advantage of this strategy is that there is no need for complex algorithms to define the optimal operating point. In addition, the power transfer in the converter happens smoothly and continuously during switching between triangular and trapezoidal modulations.

#### 3.1. Mathematical Modeling

The power transferred by the converter depends on the voltages synthesized by the active bridges. In general, phase shift  $\delta$  and inner phase shift, represented by  $\tau_1$  and  $\tau_2$ , may be present in the pulses generated by bridges. In this case, either the phase shift or the variation in the inner phase shift may be used to regulate the power flow between the bridges. In this work, the voltages synthesized by the active bridges  $v_{AC1}$  and  $v_{AC2}$  were generated through a centralized PWM, as depicted in Figure 2b.

The average value of ANPC-DAB output current  $I_{DC2}$  is obtained from phasor theory and is calculated as in (8).

$$\langle I_{DC2} \rangle_{T_s} = \frac{4 \cdot n \cdot V_{DC1} \cdot \sin \frac{\tau_1}{2} \cdot \sin \frac{\tau_2}{2} \cdot \sin \delta}{\pi^3 \cdot f_{sw} \cdot L} \quad (8)$$

where  $T_s$  is sample time and  $f_{sw} = 1/T_s$  is the switching frequency.

The average output capacitor quasi-instantaneous voltage is calculated as in (9).

$$C_2 \frac{d \langle V_{DC2} \rangle_{T_s}}{dt} = \langle I_{DC2} \rangle_{T_s} - \langle I_0 \rangle_{T_s} \quad (9)$$

where  $I_0$  and  $C_2$  are the measure output load current and the output capacitance of ANPC-DAB converter, respectively.

The discretization of (9), using the Euler method, defines the predicted voltage output (10).

$$V_{DC2}(k+1) = V_{DC2}(k) + \frac{I_{DC2} - I_0(k)}{C_2 \cdot f_{sw}} \quad (10)$$

where  $I_0(k)$  and  $V_{DC2}(k)$  are measured at time  $k$  and  $I_{DC2}$  is the defined current output derived from (8).

At instant  $(k+1)$ , there will be a synthesized voltage due to the state of the switches defined by the control at instant  $k$ . Between instants  $k$  and  $(k+1)$ , the calculation will estimate the voltages for the next cycle, i.e., at time  $(k+2)$ . Therefore, this calculation must be done using the state voltage at time  $(k+1)$ , when the control will decide the new state of the switches. To this end, a delay compensation is determined by calculating the voltage that will be synthesized at time  $(k+1)$  so that all possible predictions for instant  $(k+2)$  can be analyzed. Thus, it is necessary to calculate references for two time steps because predicting variables for only one time step is insufficient to account for the processing delay of signals.

Assuming that a sampling period's load current does not change significantly, i.e.,  $I_0(k) = I_0(k+1)$ , the  $N$  possible output voltages at time  $(k+2)$  are obtained from  $N$  output current possibilities  $I_{DC2}^N$ , as shown in (11).

$$V_{DC2}^N(k+2) = V_{DC2}(k+1) + \frac{I_{DC2}^N - I_0(k)}{C_2 \cdot f_{sw}} \quad (11)$$

### 3.2. Definition of Phase Shift and Inner Phase Shift

In this work, the main objective of the AMPC strategy is to control the output voltage  $V_{DC2}$  ensuring the lowest losses in the active bridges.

The first step is to define the value of the phase shift. The procedure consists of discretizing the entire operating range of the DAB converter into three phase-shift options, where one must be selected. The phase shift adopted is a compromise between the controller precision and the system transient response. These three phase-shift options are set based on the last angle taken by the control, as shown in (12).

$$\delta^N = [(\delta_{old} - \delta_{step}); \delta_{old}; (\delta_{old} + \delta_{step})] \quad (12)$$

where  $\delta_{old}$  is the phase shift applied at the previous instant and  $\delta_{step}$  is dynamically evaluated according to (13), the result of which determines whether to increase or decrease the transferred power [21].

$$\delta_{step} = \delta_{min} \cdot (1 + \alpha \cdot V_{adp}) \quad (13)$$

where

$$V_{adp} = \begin{cases} |V^* - V_{DC2}|; & \text{if } |V^* - V_{DC2}| \leq Vm \\ Vm; & \text{if } |V^* - V_{DC2}| > Vm \end{cases} \quad (14)$$

where  $V^*$  is the value the control will track,  $\alpha$  is a gain, the lowest phase-shift angle is  $\delta_{min}$  and the greatest value for  $V_{adp}$  is  $Vm$ .

The dynamic choice of the  $\delta_{step}$  value ensures that when the controlled variable's error is high, the response is accelerated by using the larger phase shift. On the other hand, small angles are used to increase precision when the error is small. The advantages of utilizing this adaptive technique include a low computational burden.

The next step is to define the modulation, i.e., the values of  $\tau_1$  and  $\tau_2$ . The control system will verify whether it is possible to operate with triangular modulation at the current operating point of the DAB converter, considering that this modulation promotes six soft switchings of eight commutations in one cycle. The maximum power transferred by triangular modulation occurs when the value of  $\tau_1$  reaches  $180^\circ$ . If it is not possible to transfer the required power to the DAB converter through triangular modulation, trapezoidal modulation is used instead. Trapezoidal modulation can transfer more power than triangu-

lar modulation, but in each cycle (eight commutations), there are four soft-switching events. The values of the inner phase shift will be calculated for each value of  $\delta^N$ , generating the sets  $\tau_1^N$  and  $\tau_2^N$ .

The modulation and inner phase-shift selection algorithm are shown in Figure 8.

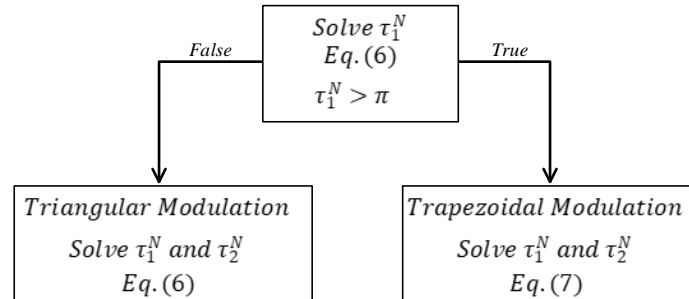


**Figure 8.** Modulation-selection algorithm.

### 3.3. Loop Compensation and Cost Function

Normally, the application of predictive control requires additional techniques to compensate for prediction errors in the controlled variables. One way to reduce these errors is to improve the mathematical model used in the control [22,23]. However, this solution increases the computational burden because it uses high-order models. Another method involves feedback compensation. This method has been used in several works [24–27]. In this work, the error compensation  $V^*$  is shown in (15). The difference between the desired and measured values of the DAB converter output voltage is added to the desired value, resulting in a compensated reference value that reduces the steady-state inaccuracy [28].

$$V^* = V_{ref} + (V_{ref} - V_{DC2}) \quad (15)$$

where  $V_{ref}$  is the desired voltage.

Finally, the optimal phase shift and its inner phase shift are defined by the smallest value of the cost function through the comparison between the desired value and the  $N = 3$  values predicted by the AMPC. The cost function  $G$  is defined in (16).

$$G = \alpha_1 \cdot G_1 + \alpha_2 \cdot G_2 \quad (16)$$

$$\begin{cases} G_1 = (V^* - V_{DC2}^N(k+2))^2 \\ G_2 = (I_{DC2}^N - I_0)^2 \end{cases} \quad (17)$$

where  $\alpha_1$  and  $\alpha_2$  are the voltage and current gains,  $V^*$  is the compensate reference,  $V_{DC2}^N$  is the  $N = 3$  possibilities of output voltage value predicted,  $I_{DC2}^N$  is the  $N = 3$  possibilities of output current value predicted, and  $I_0$  is the measure output current.

The first term,  $G_1$ , is responsible for regulating the voltage. When the output voltage is far from the target value, this term becomes dominant. As the voltage approaches the reference value, the second term,  $G_2$ , assumes a dominant role, preventing resonance in the output voltage. This oscillation occurs when the control variable ( $\delta$ ,  $\tau_1$  and  $\tau_2$ ) deviates from the desired operating point. The adjustment of  $\alpha_1$  and  $\alpha_2$  is carried out similarly to the adjustment presented in [29] and is defined as  $\alpha_1 = 1$  and  $\alpha_2 = 2$ .

In addition, a penalty is imposed on the cost function if the voltage on the input capacitors drops below 80% of the nominal value. This penalty prevents the control from selecting the  $\delta_{old}$  and  $(\delta_{old} + \delta_{step})$  phase shift presented in (12), ensuring that the converter is able to operate without drastic reduction in the voltage on the input capacitors and preventing the MOSFET's trigger driver protection from activating due to control action.

### 3.4. Flow Chart of AMPC

Figure 9 shows an overview of the AMPC for output voltage, where  $\delta_{opt}$  is the optimal phase shift and  $\tau_1(\delta_{opt})$  and  $\tau_2(\delta_{opt})$  are the inner phase shifts calculated as functions of  $\delta_{opt}$ . The ANPC-DAB converter switches are triggered by the modulation control block based on the phase shift and inner phase shift delivered by the cost function. The construction of the modulation control block is described in detail in [10].

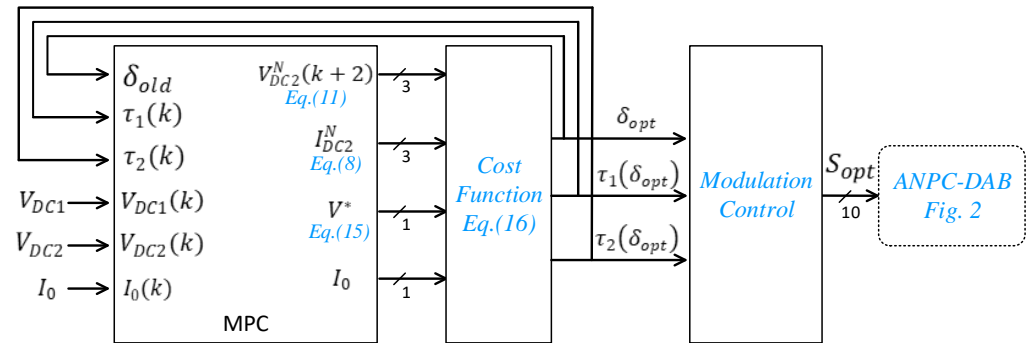


Figure 9. AMPC control strategy.

The flow chart of the proposed AMPC is presented in Figure 10, which illustrates the calculation of AMPC from control period  $k$  to  $(k + 1)$ .

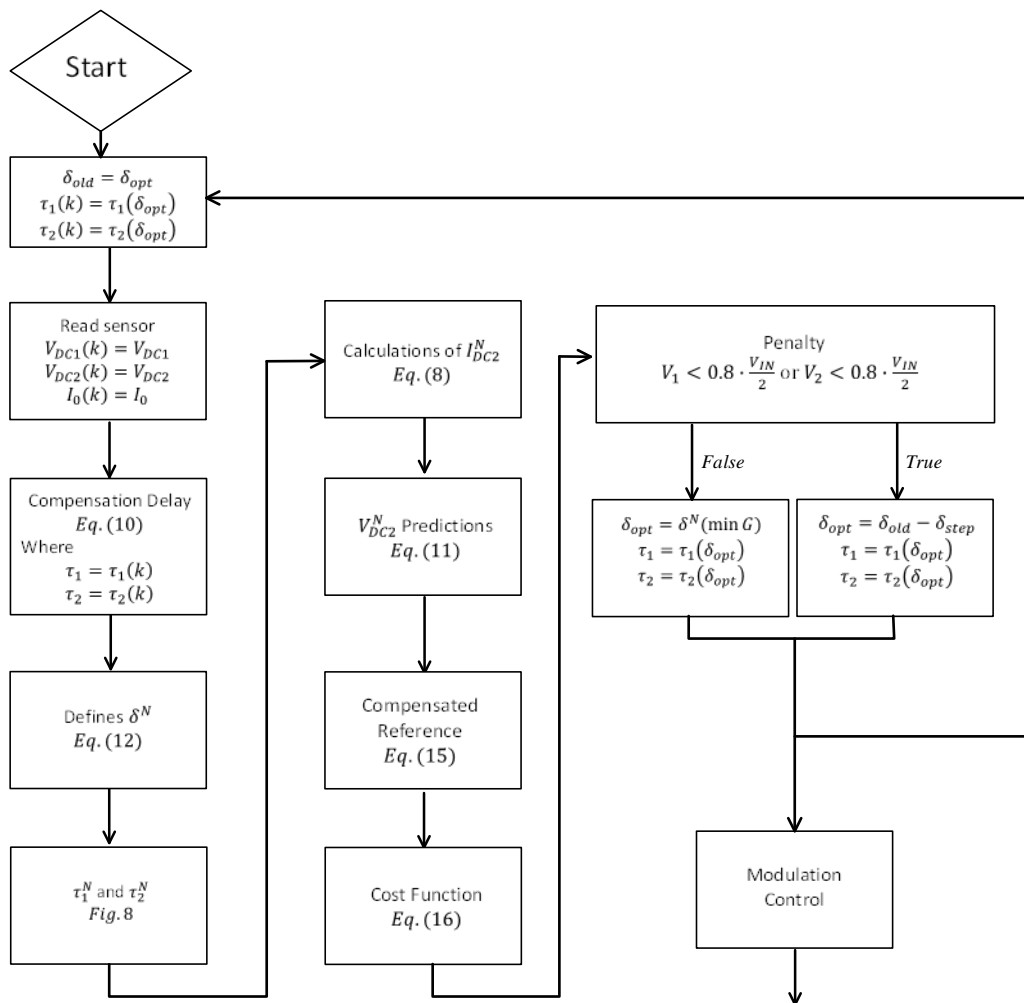


Figure 10. Flow chart of AMPC.

The process starts by reading the sensors and saving the optimal phase shift applied at instant  $k$ . The next step is to apply the compensation delay. Next, the  $\delta_{step}$  is calculated and the three phase shifts contained in  $\delta^N$  are defined. Once  $\delta^N$  is defined, the values of  $\tau_1^N$  and  $\tau_2^N$  are calculated to define the modulation for each phase shift. The output voltage is then predicted for  $N = 3$  possibilities. The next step is to apply the reference compensation and calculate the cost function for  $N = 3$  possibilities. If the voltage on the ANPC input capacitors is below 80% of the  $V_{in}/2$  value, the value of  $\delta_{opt}$  is adjusted to  $\delta_{opt} = (\delta_{old} - \delta_{step})$  with their respective  $\tau_1(\delta_{opt})$  and  $\tau_2(\delta_{opt})$ , causing the power transmitted by the DAB to be reduced. Otherwise,  $\delta_{opt}$  is adjusted so that the cost function is minimized with their respective  $\tau_1(\delta_{opt})$  and  $\tau_2(\delta_{opt})$ .

#### 4. Performance Analysis

This section details a performance analysis of the proposed AMPC control. Real-time simulation results using OPAL OP5700 were used to evaluate the proposed control. The specifications of the ANPC-DAB converter under evaluation are listed in Table 2.

**Table 2.** DAB converter parameters.

Variable	Symbol	Value
Switch Frequency	$f_{sw}$	20 kHz
Voltage Input DAB	$V_{IN}$	800 V
Voltage Output DAB	$V_{DC2}$	400 V
Rated Phase Shift	$\Phi$	45°
Rated Power Transformer	$S$	15 kVA
HFT Transformer Ratio	$n = N_1/N_2$	1.2
Leakage Inductor	$L$	32 H
Input Capacitor	$C_1 = C_2$	120 F
Output Capacitor	$C_3$	160 F
Lowest Phase-Shift Angle	$\delta_{min}$	0.05°
Gain	$\alpha$	1 rad/V
Maximum Value for $V_{adp}$	$V_m$	10 V

The ANPC-DAB converter may be affected by power-supply noise and load disturbances in real-world scenarios. Therefore, this section examines the load disturbance rejection (LDR) and source voltage disturbance rejection (SVDR), which assess the performance of the AMPC control in real-world conditions.

Another common situation in the real world involves variation in the converter parameters due to temperature. Consequently, this section evaluates the AMPC's response to variations in the inductance and capacitance of the ANPC-DAB converter. Additionally, it examines the significance of item  $G_2$  in the cost function.

The real-time simulation data were plotted using a graphical tool for better presentation. The original values were preserved, and no manipulations were carried out.

##### 4.1. Source Voltage Disturbance Rejection (SVDR)

Figure 11 illustrates the circuit used in the simulation to assess the SVDR. The input voltage of the ANPC-DAB converter was decomposed into a DC component ( $V_{DC}$ ) and an AC component ( $v_{AC}$ ). The DC component represents the nominal input voltage, while  $v_{AC}$  simulates source voltage disturbances. The experiment involved introducing a sinusoidal voltage with a peak value of 80 V in series with a DC source set at 800 V.

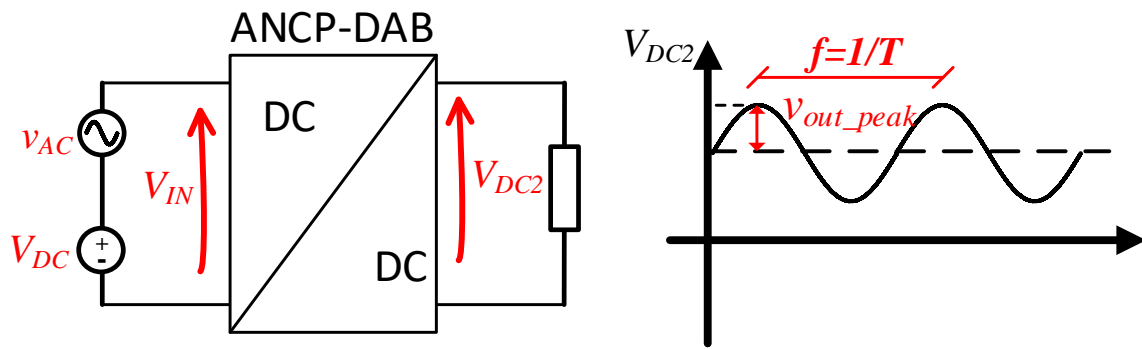


Figure 11. Real-time simulation to evaluate SVDR.

SVDR analysis involves Equation (18), where the output voltage  $V_{DC2}$  is measured for each injected frequency.

$$G_{svdr} = 20 \cdot \log \frac{v_{out\_peak}(f)}{v_{AC}(f)} \tag{18}$$

where  $v_{out\_peak}(f)$  is the ripple value of  $V_{DC2}$  at frequency  $f$  and  $v_{AC}(f) = 80\text{ V}$  for all analyzed frequencies. Figure 12 shows the frequency response for SVDR analysis.

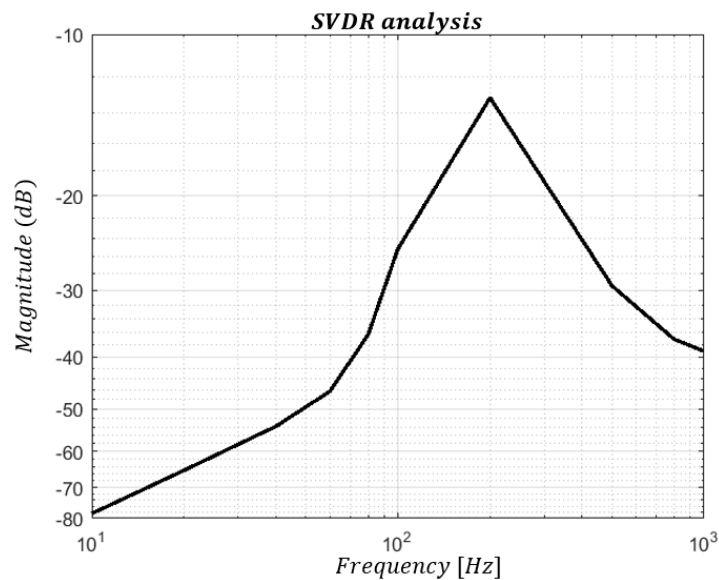


Figure 12. AMPC frequency response: SVDR analysis.

The AMPC control demonstrates exceptional performance in rejecting source disturbances. In the low-frequency band, the AMPC has a lower  $G_{svdr}$  amplitude, with a value of  $-80\text{ dB}$  at  $10\text{ Hz}$ . The most significant degradation occurs at  $200\text{ Hz}$ , with a higher  $G_{svdr}$  value of  $-13\text{ dB}$ .

#### 4.2. Load Disturbance Rejection (LDR)

When the DAB converter is applied in an SST, it can power a variety of switched loads, such as three-phase inverters, electric vehicle charging stations, and other direct current loads. Therefore, it is important to analyze the LDR of the ANPC-DAB converter. The metric used in this study was the output impedance analysis.

To illustrate this point, the converter was represented by a  $V_{out}$  source connected in series with the  $Z_{out}$  output impedance, as depicted in Figure 13.

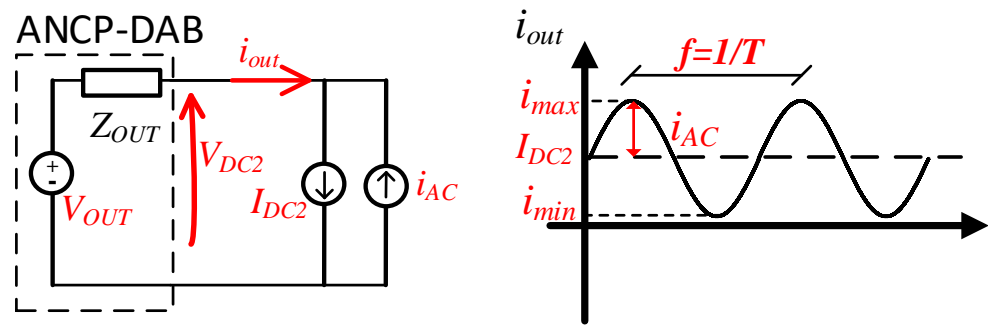


**Figure 13.** Real-time simulation to evaluate LDR.

During the analysis, the  $I_{DC2}$  current was set to 8 A and the current  $i_{AC}$  was added as a disturbance to simulate the load disturbance. The  $i_{AC}$  value was chosen to induce a change of modulation. The output impedance was then calculated using Equation (19).

$$Z_{out} = \frac{v_{out\_peak}(f)}{i_{AC}(f)} \quad (19)$$

where  $v_{out\_peak}$  is the ripple value of  $V_{DC2}$  at frequency  $f$  and  $i_{AC}(f) = 7/\sqrt{2}A$  for all analyzed frequencies. Figure 14 shows the frequency response for LDR analysis.

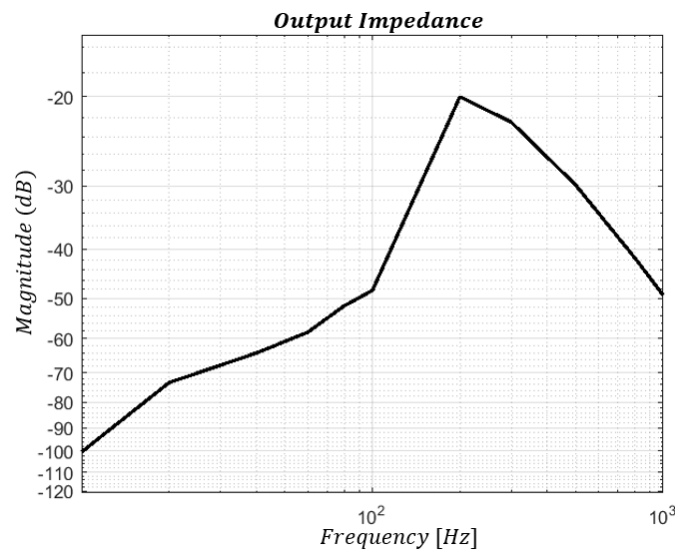


**Figure 14.** AMPC Frequency Response: Real-time simulation results of LDR analysis of the ANPC-DAB converter.

The AMPC control exhibits excellent performance in load disturbance rejection. The output impedance ( $Z_{out}$ ) increases from  $-100$  dB to  $-20$  dB in the frequency range of 10 Hz to 200 Hz.

#### 4.3. Variations of Circuit Parameters

This section evaluates the robustness of the AMPC algorithm against variations in the ANPC-DAB converter parameters. The analysis is particularly significant because the converter parameters can change in real-world scenarios [7]. For this experiment, the voltage  $V_{DC2}$  was varied from 380 V to 400 V, considering a variation of  $\pm 50\%$  in the values of  $L$  and  $C_3$ . Figure 15a,b depicts the behavior of the output voltage in response to changes in capacitance  $C_3$  and inductance  $L$ , respectively.

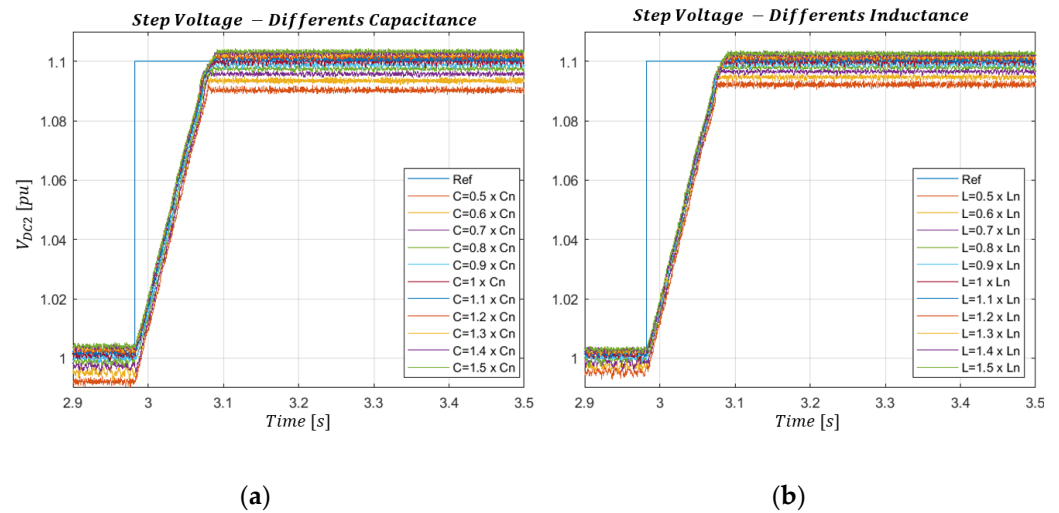


**Figure 15.** Behavior of the output voltage for variation parameters (a) inductance,  $L$  (b) capacitance,  $C_3$ .

Upon analysis of Figure 15, it is apparent that variations in capacitance and inductance have minimal impacts when the circuit is in a steady state. Table 3 presents the primary quantitative results of the ANPC-DAB converter for all the analyzed scenarios. The mean absolute error (MAE) of the  $V_{DC2}$  voltages for each scenario is calculated using Equation (20), where  $M$  denotes the total number of collected samples, and  $y_k^*$  and  $y_k$  represent the reference and measured signals, respectively, at instant  $k$ .

$$MAE = \frac{\sum_{k=1}^M |y_k^* - y_k|}{M} \quad (20)$$

**Table 3.** Quantitative analysis of output voltage.

Inductor	MAE ( $V_{DC2}$ )	Capacitor	MAE ( $V_{DC2}$ )
$L_r = 0.5 \cdot L$	6.10 V (1.52%)	$C_r = 0.5 \cdot C_3$	6.96 V (1.74%)
$L_r = 0.6 \cdot L$	5.19 V (1.29%)	$C_r = 0.6 \cdot C_3$	5.75 V (1.44%)
$L_r = 0.7 \cdot L$	4.56 V (1.14%)	$C_r = 0.7 \cdot C_3$	4.95 V (1.23%)
$L_r = 0.8 \cdot L$	4.05 V (1.01%)	$C_r = 0.8 \cdot C_3$	4.27 V (1.06%)
$L_r = 0.9 \cdot L$	3.69 V (0.92%)	$C_r = 0.9 \cdot C_3$	3.80 V (0.95%)
$L_r = 0.1 \cdot L$	3.52 V (0.88%)	$C_r = 0.1 \cdot C_3$	3.53 V (0.88%)
$L_r = 1.1 \cdot L$	3.57 V (0.89%)	$C_r = 1.1 \cdot C_3$	3.61 V (0.90%)
$L_r = 1.2 \cdot L$	3.71 V (0.92%)	$C_r = 1.2 \cdot C_3$	3.78 V (0.94%)
$L_r = 1.3 \cdot L$	3.86 V (0.97%)	$C_r = 1.3 \cdot C_3$	3.94 V (0.98%)
$L_r = 1.4 \cdot L$	3.99 V (0.99%)	$C_r = 1.4 \cdot C_3$	4.12 V (1.03%)
$L_r = 1.5 \cdot L$	4.09 V (1.02%)	$C_r = 1.5 \cdot C_3$	4.25 V (1.06%)

The results show that the control is more robust to inductor variation, yielding an MAE of 1.52%. For capacitor variations, the MAE was 1.74%.

#### 4.4. Cost-Function Analysis

As mentioned earlier, the term  $G_2$  in the cost function is intended to reduce the resonance at the output voltage  $V_{DC2}$ . To demonstrate its effectiveness, the  $G_2$  term was negated by setting  $a_2 = 0$  during a real-time simulation, and the measured resonance frequency in this case was 1 kHz.

Figure 16 shows the impact of the  $G_2$  term on the behavior of the output voltage of the DAB converter, and it is clear that steady-state resonance is attenuated. This resonance reduction results in a decrease in acoustic noise emitted by the transformer, as well as a reduction in transformer losses.

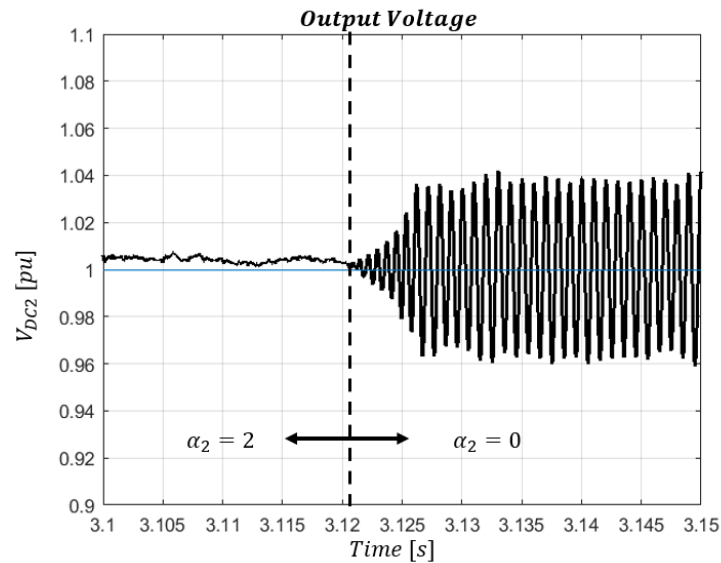


**Figure 16.** Verification of the effectiveness of  $G_2$ .

## 5. Experimental Results

The AMPC control strategy was validated in a downscaled prototype in an ANPC-DAB converter operating at 8 kW 20 kHz 800 V/400 V. The experimental setup is shown in Figure 17. The platform consists of the ANPC-DAB converter, control system, load simulator and DC source.

The ANPC-DAB converter employs isolated voltage sensors, LEM DVC 1000-P (two for the ANPC input capacitors and one for the output voltage), and a current sensor, LEM LA 55-P, to monitor the output current. The ANPC and H-bridge were built using CREE CAS120M12BM2 modules, with three modules for ANPC and two modules for the H-bridge. Capacitor M119550731 77 G, 10  $\mu$ F, 1.3 kV, forms one of the input capacitor banks (two blocks of 12 capacitors— $C_1 = C_2 = 120 \mu\text{F}$ ) and output capacitor banks (16 capacitors— $C_3 = 160 \mu\text{F}$ ). The high-frequency transformer (HFT) has a turns ratio of  $n = 1.2$  and a power of 15 kVA.

The ANPC-DAB output load was simulated using a Cinergia GE&EL-50, a power electronics device that is capable of simulating both AC and DC electrical networks. In this study, the device was configured to simulate resistive loads. To power the converter, two ePower model SPS 15 kW programmable DC sources were used.

The control system is based on the OPAL OP5700-RCP/HIL Virtex7 FPGA-based Real-Time Simulator, which is equipped with an Intel Xeon E5 processor with 8 cores, 3.2 GHz frequency, and 20 MB cache. The test bench was developed at Laboratory of Electronic Engineering Applied to Renewable Energies, University of Alcalá de Henares, Madrid, Spain. The four analog signals from the DAB sensors are received and processed by OPAL, which generates the pulses to trigger the MOSFETs. The trigger signal is transmitted over fiber optics between OPAL and ANPC-DAB.

This study includes steady-state and transient-behavior analysis, as well as assessment of the computational burden. The steady-state performance of the ANPC-DAB converter was evaluated in terms of output voltage, AC voltages, inductor current, and global losses. Global losses were calculated by measuring the input and output power when the converter operates in steady state.

The transient behavior for  $d > 1$  using AMPC control was analyzed observing the converter output voltage. In addition, all experiments were performed with traditional MPC, referred to here as MPC, for comparisons with AMPC.

The goal was to simulate the behavior of the DC-DC stage of an SST in which one side operates at 800 V and the other at 400 V, with the ANPC-DAB converter stabilizing the voltage on the 400 V side.

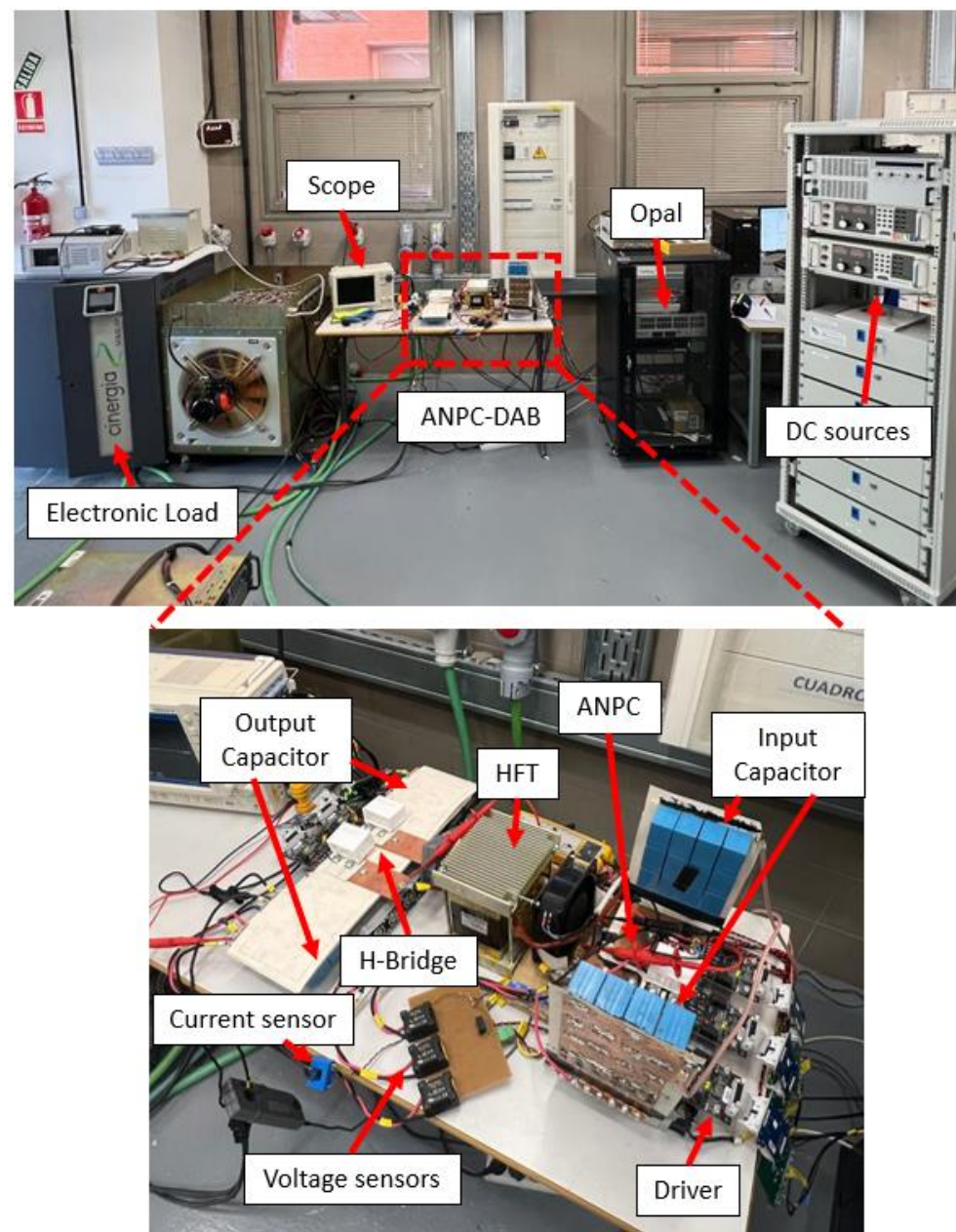


**Figure 17.** Experimental setup.

### 5.1. Computational Burden

The computation time of the proposed AMPC was measured with OPAL resources. The AMPC controller takes  $9.5 \mu\text{s}$  to run, while the time to run MPC was  $8.7 \mu\text{s}$ . The AMPC does not use complex optimization techniques, instead requires almost the same time as the traditional MPC. When a 20 kHz switching frequency is utilized,  $50 \mu\text{s}$  is available in a single sampling period. Thus, there is enough time to implement other functionalities, such as protections, MODBUS communication etc.

### 5.2. Steady-State Analysis

The steady-state analysis aims to compare the overall performance of the converter using AMPC to that using MPC. In the first test, the load was set to 7.36 kW. At this point, the AMPC operates with triangular modulation. Waveforms of  $v_{AC1}(t)$ ,  $v_{AC2}(t)$  and  $I_L(t)$  using AMPC and MPC are shown in Figures 18a and 18b, respectively.

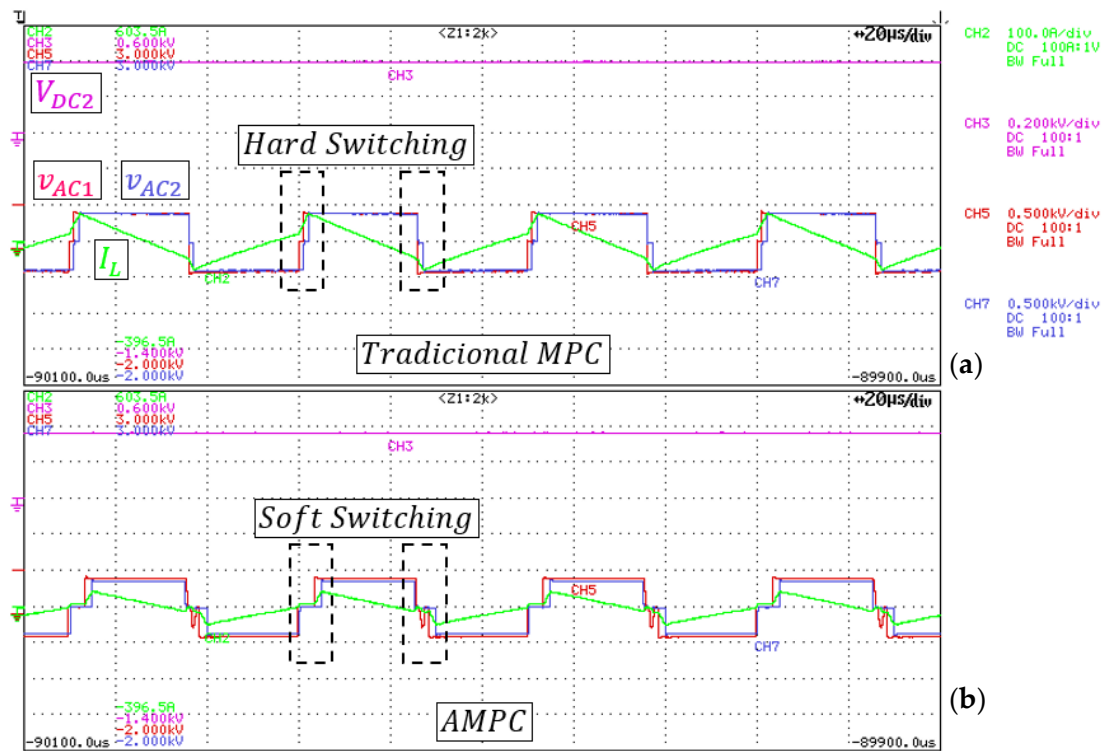


Figure 18. Waveforms of  $v_{AC1}(t)$ ,  $v_{AC2}(t)$  and  $I_L(t)$ . (a) MPC Control (b) AMPC Control.

The second test load was set to 8.4 kW. At this point, the AMPC operates with trapezoidal modulation. Waveforms of  $v_{AC1}(t)$ ,  $v_{AC2}(t)$  and  $I_L(t)$  using MPC and AMPC are shown in Figures 19a and 19b, respectively.

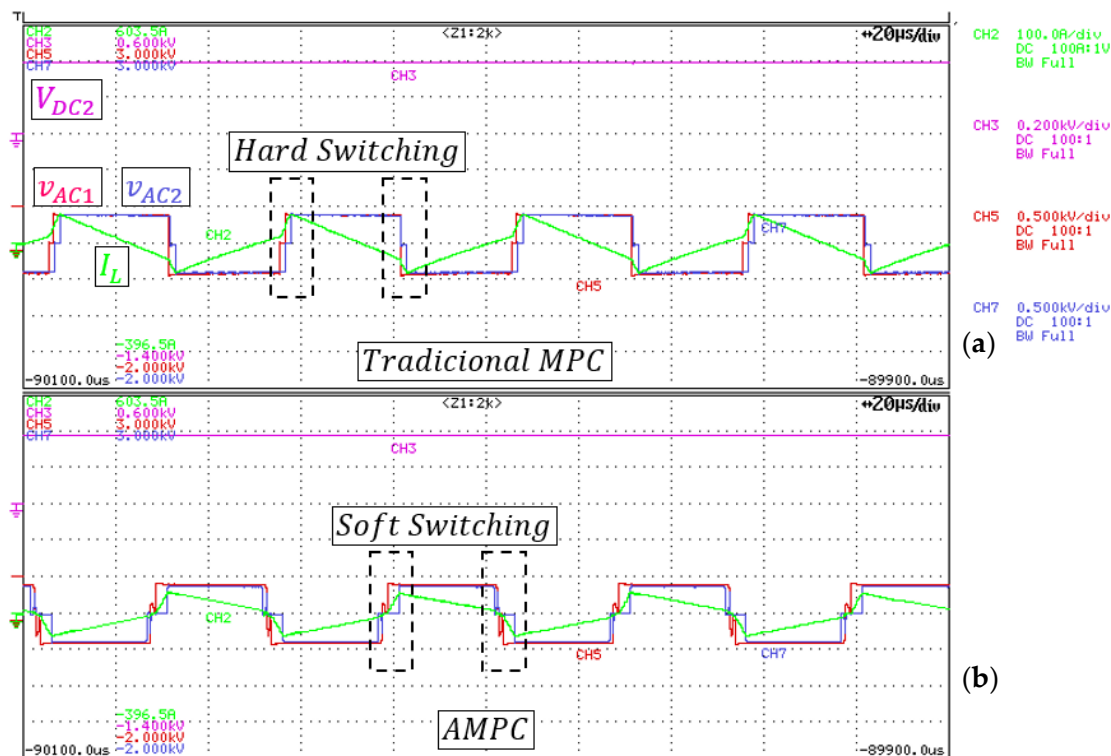


Figure 19. Waveforms of  $v_{AC1}(t)$ ,  $v_{AC2}(t)$ , and  $I_L(t)$ . (a) MPC control (b) AMPC control.

Qualitatively, Figures 18b and 19b show that the converter operating with the MPC has hard switching in state changes ( $P$ ,  $Z$ , and  $N$ ), whereas this change occurs in the presence of current, dissipating more power in the switches. In contrast, the AMPC control causes the converter to operate with soft switching, i.e., six soft switchings out of the eight commutations in one cycle when the control chooses triangular modulation and four soft switchings out of the eight commutations in one cycle when the control chooses trapezoidal modulation.

Table 4 presents values of input voltage, output voltage, input current, and output current for the two operating points mentioned above with MPC and AMPC control.

**Table 4.** Global losses in ANPC-DAB for AMPC and MPC control.

MPC	AMPC
<i>Load = 7.36 kW</i>	
$V_{IN} = 800.8 \text{ V}$	$V_{IN} = 800.6 \text{ V}$
$I_{IN} = 9.75 \text{ A}$	$I_{IN} = 9.53 \text{ A}$
$V_{DC2} = 396.3 \text{ V}$	$V_{DC2} = 394.5 \text{ V}$
$I_{DC2} = 18.23 \text{ A}$	$I_{DC2} = 18.13 \text{ A}$
$\eta = 92.53\%$	$\eta = 93.77\%$
<i>Load = 8.4 kW</i>	
$V_{IN} = 800.6 \text{ V}$	$V_{IN} = 800.5 \text{ V}$
$I_{IN} = 11.02 \text{ A}$	$I_{IN} = 10.83 \text{ A}$
$V_{DC2} = 396.2 \text{ V}$	$V_{DC2} = 394.8 \text{ V}$
$I_{DC2} = 20.8 \text{ A}$	$I_{DC2} = 20.71 \text{ A}$
$\eta = 93.37\%$	$\eta = 94.33\%$

The proposed AMPC control demonstrated accurate response, with less than 1.4% error on the output voltage mean value. This control increased the converter's global efficiency without changing the hardware or increasing computational efforts. In microgrid applications, where the SST operates at low loads for extended periods, high efficiency is essential. The AMPC control strategy can save approximately 600 kWh of energy in one year of operation (8.4 kW, 18 h of low load per day), equivalent to the monthly consumption of three houses with a 200 kWh usage, simply through use of the AMPC control.

### 5.3. Transient Analysis

The transient behavior of the AMPC control was analyzed for load and voltage step on the converter. The MPC control was subjected to the same analyses for comparison purposes.

In the first experiment, the load was changed from 7.36 kW to 8.40 kW to evaluate the response of the AMPC to a modulation change, which is a critical situation. In order to visualize the chosen modulation on the scope within other DAB variables, an analog output was used, where 3 V indicates triangular modulation, 4 V indicates trapezoidal modulation, and 5 V indicates SPS modulation (used in MPC).

Figures 20 and 21 show the behavior of the output voltage for AMPC and the MPC controls, respectively, where the purple, blue, and yellow lines are the  $V_{DC2}$  voltage, the  $I_{DC2}$  current, and the modulation used by the control, respectively.

The AMPC control can keep the output voltage stable and choose between triangular and trapezoidal modulations according to the operating point, ensuring better converter efficiency. The response time was less than 282 ms with an overshoot of less than 6.86%. Comparing traditional MPC with AMPC, the differences in transient behavior are small. The summarized results of the experiment are shown in Table 5.

In the second experiment, the  $V_{ref}$  voltage was changed from 380 V to 400 V. Figures 22 and 23 show the behavior of the AMPC and the MPC controls, respectively, where the purple, blue, yellow, and red lines are the  $V_{DC2}$  voltage, the  $I_{DC2}$  current, the modulation used by the control, and the desired value for the output voltage  $V_{ref}$ , respectively.

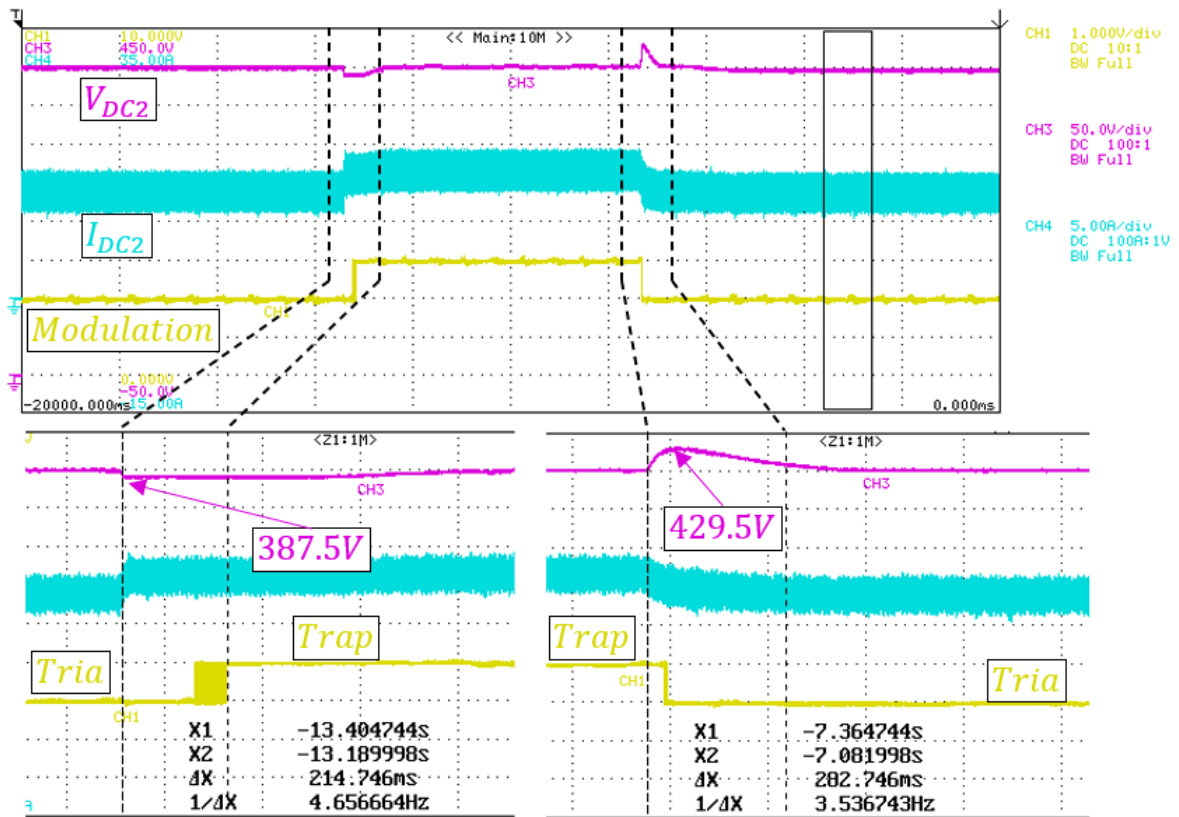


Figure 20. AMPC performance under a load step.

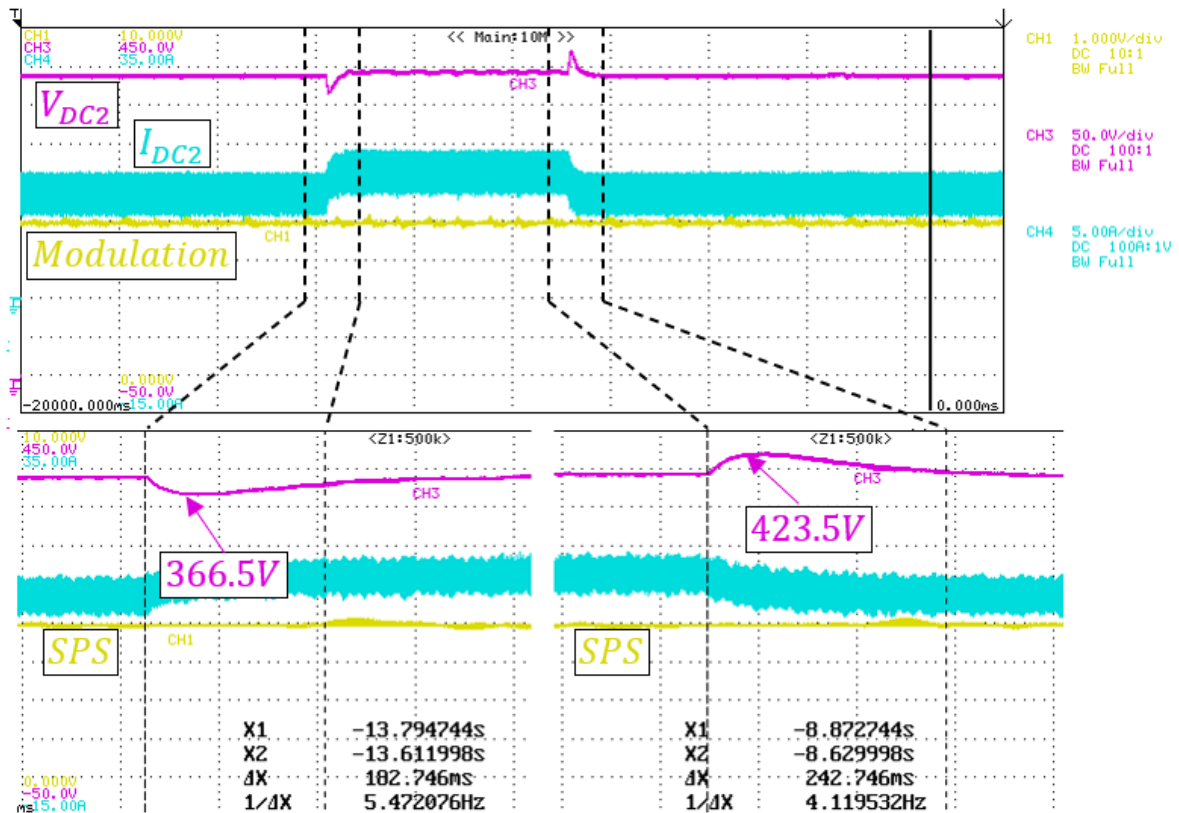


Figure 21. MPC performance under a load step.

Table 5. Load-step results: comparison of AMPC × MPC.

Transition	AMPC Settling Time	MPC Settling Time	AMPC Overshoot	MPC Overshoot
7.36 kW → 8.40 kW	214 ms	182 ms	$\frac{(400-387.5)}{400} = 3.1\%$	$\frac{(400-366.5)}{400} = 8.4\%$
8.40 kW → 7.36 kW	282 ms	242 ms	$\frac{(400-429.5)}{400} = -7.4\%$	$\frac{(400-423.5)}{400} = -5.9\%$

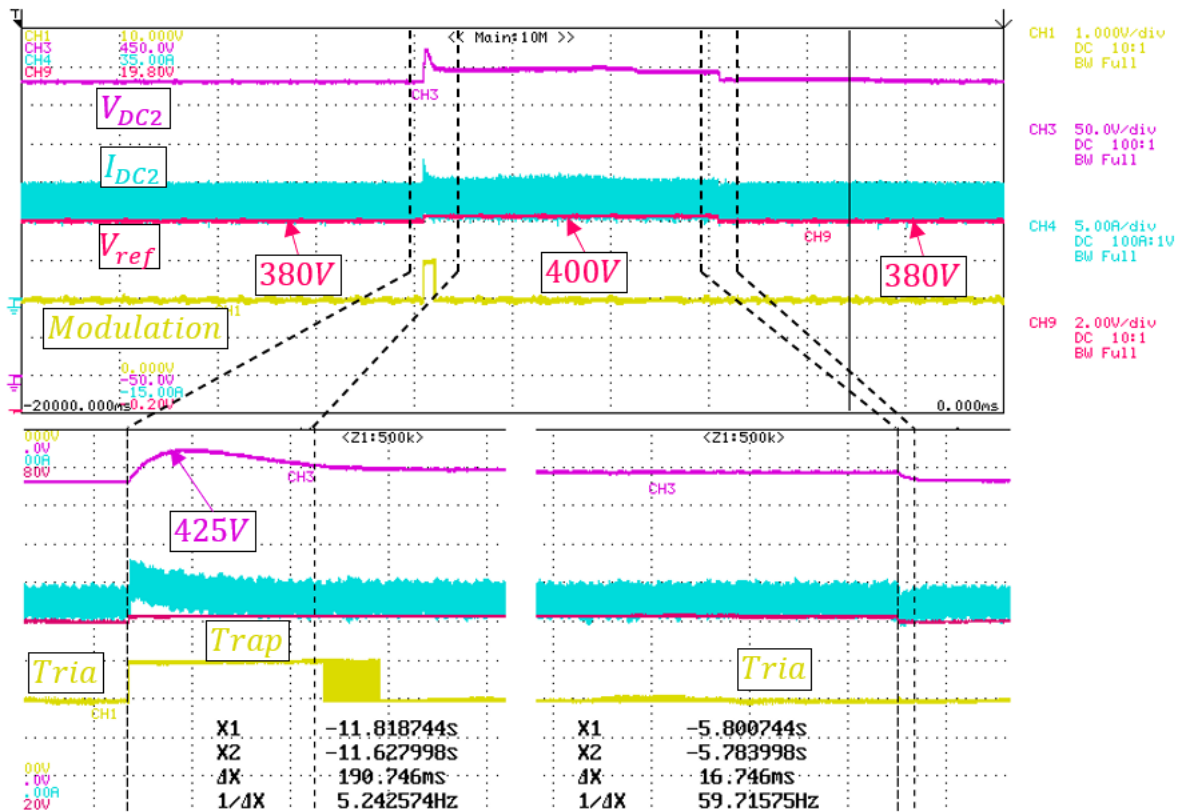


Figure 22. AMPC performance under a  $V_{ref}$  step.

In this scenario, the AMPC strategy dynamically changes the phase shift and inner phase shift in order to charge the output capacitor so that the  $V_{DC2}$  voltage reach the new requested reference value.

AMPC and MPC showed similar performance. However, in the transition  $V_{ref} = 400V \rightarrow 380V$ , there was no undervoltage and the settling time was much shorter than in the MPC. The summarized results of the experiment are shown in Table 6.

Table 6. Voltage step results: comparison of AMPC and MPC.

Transition	AMPC Settling Time	MPC Settling Time	AMPC Overshoot	MPC Overshoot
380 V → 400 V	190 ms	178 ms	$\frac{(400-425)}{400} = -6.3\%$	$\frac{(400-440)}{400} = -10\%$
400 V → 380 V	16 ms	358 ms	$\frac{(380-380)}{380} = 0.00\%$	$\frac{(380-346)}{380} = 8.95\%$

Unlike a simulated environment, the converter’s transient power transfer is limited, which delays the response time in relation to other topologies. The insertion of the penalty in the cost function prevents the ANPC input capacitor from discharging to levels that cause the MOSFET’s protection trigger drivers to activate.

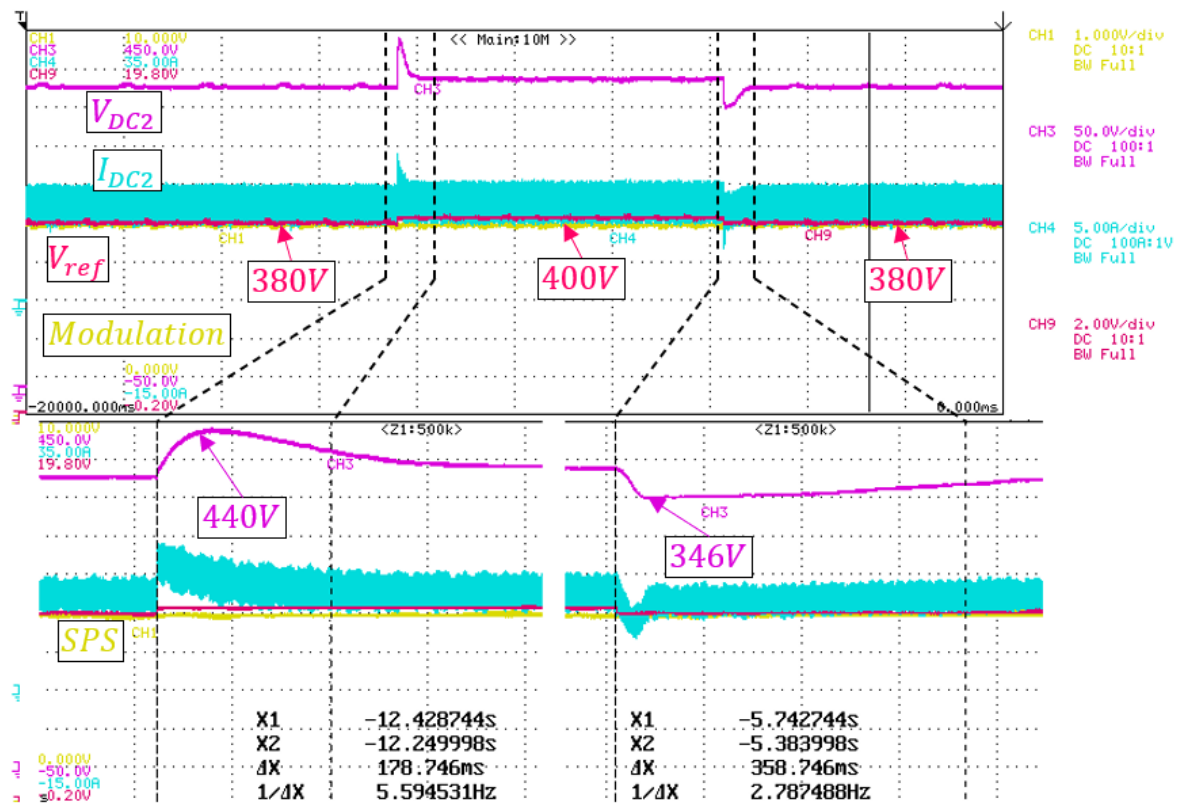


Figure 23. MPC performance under a  $V_{ref}$  step.

## 6. Discussion

The DAB converter has many advantages for use in SSTs, including galvanic isolation, bidirectional power flow, high power density, and the ability to operate as a buck or boost with ZVS over a wide range. However, low loads and high voltages can pose challenges to its efficiency and operation capacity. To address this difficulty, multilevel topologies such as the ANPC-DAB can be used. In this topology, ANPC is applied on the high-voltage side and an H-bridge is used on the low-voltage side. Experiments were conducted on an 8 kW 20 kHz 800 V/400 V prototype.

The traditional control method used in the DAB converter controls only the phase shift, limiting its efficiency at low loads. To improve efficiency at low loads, different modulations can be used to enable soft switching throughout the operating range. However, these solutions require the selection of voltage values for the converter's active bridges, which involves complex optimization methods that can increase computational costs and hinder practical application.

MPC is an advanced technique used in many electrical systems. Unlike conventional control, it predicts the system's future behavior using mathematical modeling and calculates an optimal control signal to maintain the desired output. To enhance efficiency at low loads, AMPC control, which employs triangular and trapezoidal modulations, is used. The natural transition between these modulations results in a gradual change in the inductor's current waveform from triangular to trapezoidal or vice versa. This method is used to obtain the highest efficiency when the DAB converter operates at low loads.

Real-time simulation was used to evaluate the frequency response and robustness of the AMPC applied to the ANPC-DAB topology. The converter attenuates voltage-source noise by  $-80$  dB at low frequencies, with the worst case at 200 Hz, at which it attenuates the disturbance by  $-13$  dB. Additionally, AMPC offers low output impedance, allowing for high-intensity output current without significant voltage drops, which is essential for maintaining output current stability in applications with load variations.

Robustness tests were conducted by varying the power transfer inductance and output capacitance. There are several approaches to designing predictive controllers that are robust to converter parameter variations. In this work, the reference is adjusted to ensure lower error when the converter operates in steady state. Mean absolute error (MAE) values of 1.54% and 1.74% were obtained for a 50% variation in the nominal values for the inductor and capacitor, respectively.

The impact of the  $G_2$  term in the cost function on the output voltage was demonstrated. When  $\alpha_2 = 0$ , a resonance occurs in the output voltage, even in steady state. Resonance can cause system instability, low performance, electrical noise, and electromagnetic interference, which can affect nearby electronic systems. Therefore, the importance of the  $G_2$  term in reducing oscillations in the system is evident.

Experimental results from the prototype indicate a significant improvement in converter efficiency with the AMPC control, achieving 94.33% at 8.4 kW and 93.77% at 7.36 kW in steady state, compared to 93.37% and 92.53%, respectively, with the MPC. While the dynamic response of the AMPC control did not differ significantly from that of the MPC, the MPC was faster and the AMPC showed smaller overshoots in most of the tests.

Finally, an important advantage of AMPC is that it eliminates the need for complex optimization processes to choose the phase shift and inner phase shift, while also avoiding the need for intense computational efforts. This study shows that the processing time difference between MPC and AMPC is only 0.7  $\mu$ s.

For future work, the control methodology discussed in this study can be applied to input series output parallel (ISOP) structures to verify the energy efficiency of the structure and evaluate the control behavior for transient situations and steady-state operation.

## 7. Conclusions

The present article proposes the application of the advanced AMPC control technique in the ANPC-DAB topology. This topology enables the converter to operate at high voltages, providing an alternative to ISOP structures, which operate in series and parallel.

Several real-time simulated analyses have shown that the AMPC control has high capacity for voltage-source noise rejection and exhibits low output impedance. Additionally, dynamic reference adjustment has improved the control's robustness to variations in converter parameters.

The experimental results from the prototype showed excellent dynamic and steady-state performance. The AMPC exhibited dynamic response similar to that of the MPC. However, in steady state, the efficiency of the converter was significantly improved with use of the AMPC, reaching 94.33% at 8.4 kW and 93.77% at 7.36 kW in steady state, compared to 93.37% and 92.53%, respectively, without the AMPC. Additionally, the control achieved error rates below 1.4% in relation to the desired value.

Despite the benefits of using AMPC, the computational cost was not significantly increased compared to MPC. The processing time was measured using OPAL resources, which showed that the MPC processing time was 8.7  $\mu$ s, while that of the AMPC was 9.5  $\mu$ s. Considering that the processor has 50  $\mu$ s available ( $T = 1/20$  kHz), applying AMPC leaves enough time for other applications, such as protections and data communication.

**Author Contributions:** Conceptualization, A.N. and R.F.; Formal analysis, A.N. and R.F.; Investigation, D.M.; Methodology, A.N.; Software, D.M. and E.B.; Supervision, E.B., L.E. and W.S.; Validation, A.N. and D.M.; Writing—original draft, A.N. and A.A.; Writing—review & editing, A.A., L.E. and W.S. All authors have read and agreed to the published version of the manuscript.

**Funding:** This research was funded by Espírito Santo Research and Innovation Support Foundation—FAPES (grant number 514/2021, 382/2021, 1024/2022, 1068/2022 and 336/2023), National Council for Scientific and Technological Development—CNPq (grant number 311848/2021-4) and Ministerio de Ciencia e Innovación (grant numbers TED2021-130610B-C21 and PID2021-125628OB-C22).

**Data Availability Statement:** Data are contained within the article.

**Acknowledgments:** Thanks to the Alcalá University and Federal University of Espírito Santo for providing equipment, physical structure, support, and assistance from professors; and to the Federal Institute of Espírito Santo for allowing me to use my working hours to conduct research with other educational institutions.

**Conflicts of Interest:** The authors declare no conflict of interest.

## References

1. Ruiz, F.; Perez, M.A.; Espinosa, J.R.; Gajowik, T.; Stynski, S.; Malinowski, M. Surveying Solid-State Transformer Structures and Controls: Providing Highly Efficient and Controllable Power Flow in Distribution Grids. *IEEE Ind. Electron. Mag.* **2020**, *14*, 56–70. [[CrossRef](#)]
2. She, X.; Huang, A.Q.; Burgos, R. Review of Solid-State Transformer Technologies and Their Application in Power Distribution Systems. *IEEE J. Emerg. Sel. Top. Power Electron.* **2013**, *1*, 186–198. [[CrossRef](#)]
3. Huber, J.E.; Kolar, J.W. Applicability of Solid-State Transformers in Today's and Future Distribution Grids. *IEEE Trans. Smart Grid* **2017**, *10*, 317–326. [[CrossRef](#)]
4. Gu, Q.; Yuan, L.; Yi, S.; Nie, J.; Zhao, Z. Active Selection of Current Commutation Loop for Hybrid Three-Level Dual Active Bridge DC-DC Converter with TPS Control. In Proceedings of the 2019 IEEE 10th International Symposium on Power Electronics for Distributed Generation Systems (PEDG), Xi'an, China, 3–6 June 2019; IEEE: Piscataway, NJ, USA, 2019; pp. 155–161.
5. Nabae, A.; Takahashi, I.; Akagi, H. A new neutral-point-clamped PWM inverter. *IEEE Trans. Ind. Appl.* **1981**, *5*, 518–523. [[CrossRef](#)]
6. Bruckner, T.; Bernet, S.; Guldner, H. The active NPC converter and its loss-balancing control. *IEEE Trans. Ind. Electron.* **2005**, *52*, 855–868. [[CrossRef](#)]
7. Bruckner, T.; Bernet, S. Loss Balancing in Three-Level Voltage Source Inverters Applying Active NPC Switches. In Proceedings of the 2001 IEEE 32nd Annual Power Electronics Specialists Conference (IEEE Cat. No. 01CH37230), Vancouver, BC, Canada, 17–21 June 2001; IEEE: Piscataway, NJ, USA, 2001; Volume 2.
8. De Doncker, R.W.; Divan, D.M.; Kheraluwala, M.H. A three-phase soft-switched high-power-density DC/DC converter for high-power applications. *IEEE Trans. Ind. Appl.* **1991**, *27*, 63–73. [[CrossRef](#)]
9. Schibli, N. Symmetrical Multilevel Converters with Two Quadrant DC-DC Feeding. Thesis, École Polytechnique Fédérale de Lausanne, Lausanne, Switzerland, 2000.
10. Nardoto, A.; Amorim, A.; Santana, N.; Bueno, E.; Encarnaçao, L.; Santos, W. Adaptive Model Predictive Control for DAB Converter Switching Losses Reduction. *Energies* **2022**, *15*, 6628. [[CrossRef](#)]
11. Hu, J.; Cui, S.; De Doncker, R.W. Natural boundary transition and inherent dynamic control of a hybrid-mode-modulated dual-active-bridge converter. *IEEE Trans. Power Electron.* **2021**, *37*, 3865–3877. [[CrossRef](#)]
12. Rauf, U.; Schütt, M.; Eckel, H.G. Model Predictive Control for Space Vector Modulation of a Three-Level ANPC Inverter for Efficient Loss Distribution and Neutral Point Balancing. In Proceedings of the 2019 21st European Conference on Power Electronics and Applications (EPE'19 ECCE Europe), Genova, Italy, 3–5 September 2019; IEEE: Piscataway, NJ, USA, 2019.
13. Deng, Y.; Li, J.; Shin, K.H.; Viitanen, T.; Saedifard, M.; Harley, R.G. Improved modulation scheme for loss balancing of three-level active NPC converters. *IEEE Trans. Power Electron.* **2016**, *32*, 2521–2532. [[CrossRef](#)]
14. Guan, Q.X.; Zhang, Y.; Zhao, H.B.; Kang, Y. Optimized Switching Strategy for ANPC–DAB Converter Through Multiple Zero States. *IEEE Trans. Power Electron.* **2021**, *37*, 2885–2898. [[CrossRef](#)]
15. Kumar, S.; Akin, B.; Gohil, G. EMI Performance of Active Neutral Point Clamped Phase Leg for Dual Active Bridge DC–DC Converter. *IEEE Trans. Ind. Appl.* **2021**, *57*, 6093–6104. [[CrossRef](#)]
16. dos Santos, W.M.; Martins, D.C. Introdução ao conversor DAB monofásico. *Eletrônica Potência* **2014**, *19*, 36–46.
17. Shi, H.; Wen, H.; Chen, J.; Hu, Y.; Jiang, L.; Chen, G.; Ma, J. Minimum-backflow-power scheme of DAB-based solid-state transformer with extended-phase-shift control. *IEEE Trans. Ind. Appl.* **2018**, *54*, 3483–3496. [[CrossRef](#)]
18. Shao, S.; Jiang, M.; Ye, W.; Li, Y.; Zhang, J.; Sheng, K. Optimal phase-shift control to minimize reactive power for a dual active bridge DC–DC converter. *IEEE Trans. Power Electron.* **2019**, *34*, 10193–10205. [[CrossRef](#)]
19. Gu, Q.; Yuan, L.; Nie, J.; Sun, J.; Zhao, Z. Current stress minimization of dual-active-bridge DC–DC converter within the whole operating range. *IEEE J. Emerg. Sel. Top. Power Electron.* **2018**, *7*, 129–142. [[CrossRef](#)]
20. Kheraluwala, M.N.; Gascoigne, R.W.; Divan, D.M.; Baumann, E.D. Performance characterization of a high-power dual active bridge DC-to-DC converter. *IEEE Trans. Ind. Appl.* **1992**, *28*, 1294–1301. [[CrossRef](#)]
21. Chen, L.; Shao, S.; Xiao, Q.; Tarisciotti, L.; Wheeler, P.W.; Dragičević, T. Model predictive control for dual-active-bridge converters supplying pulsed power loads in naval DC micro-grids. *IEEE Trans. Power Electron.* **2019**, *35*, 1957–1966. [[CrossRef](#)]
22. Eremeeva, A.M.; Ilyushin, Y.V. Automation of the control system for drying grain crops of the technological process for obtaining biodiesel fuels. *Sci. Rep.* **2023**, *13*, 14956. [[CrossRef](#)]
23. Ilyushin, Y.V. Development of a process control system for the production of high-paraffin oil. *Energies* **2022**, *15*, 6462. [[CrossRef](#)]
24. Dutta, S.; Hazra, S.; Bhattacharya, S. A digital predictive current-mode controller for a single-phase high-frequency transformer-isolated dual-active bridge DC-to-DC converter. *IEEE Trans. Power Electron.* **2016**, *63*, 5943–5952. [[CrossRef](#)]

25. Shen, K.; Feng, J.; Zhang, J. Finite control set model predictive control with feedback correction for power converters. *CES Trans. Electr. Mach. Syst.* **2018**, *2*, 312–319. [[CrossRef](#)]
26. Aguilera, R.P.; Lezana, P.; Quevedo, D.E. Finite-control-set model predictive control with improved steady-state performance. *IEEE Trans. Ind. Inform.* **2012**, *9*, 658–667. [[CrossRef](#)]
27. Du, G.; Li, J.; Liu, Z. The Improved Model Predictive Control Based on Novel Error Correction between Reference and Predicted Current. In Proceedings of the 2018 IEEE Applied Power Electronics Conference and Exposition (APEC), San Antonio, TX, USA, 4–8 March 2018; IEEE: Piscataway, NJ, USA, 2018.
28. Quevedo, D.E.; Aguilera, R.P.; Pérez, M.A.; Cortés, P. Finite Control Set MPC of an AFE Rectifier with Dynamic References. In Proceedings of the 2010 IEEE International Conference on Industrial Technology, Via del Mar, Chile, 14–17 March 2010; IEEE: Piscataway, NJ, USA, 2010.
29. Dragicevic, T.; Novak, M. Weighting Factor Design in Model Predictive Control of Power Electronic Converters: An Artificial Neural Network Approach. *IEEE Trans. Ind. Electron.* **2018**, *66*, 8870–8880. [[CrossRef](#)]

**Disclaimer/Publisher’s Note:** The statements, opinions and data contained in all publications are solely those of the individual author(s) and contributor(s) and not of MDPI and/or the editor(s). MDPI and/or the editor(s) disclaim responsibility for any injury to people or property resulting from any ideas, methods, instructions or products referred to in the content.